Enhanced Southern Ocean CO$_2$ outgassing as a result of stronger and poleward shifted southern hemispheric westerlies

Laurie C. Menviel[1,2*], Paul Spence[2,3], Andrew E. Kiss[4,5], Matthew A. Chamberlain[3,6], Hakase Hayashida[3,7], Matthew H. England[1,2], and Darryn Waugh[8,9]

[1]Climate Change Research Centre, University of New South Wales, Sydney, Australia

[2]The Australian Centre for Excellence in Antarctic Science, University of Tasmania, Hobart, Tasmania 7001, Australia

[3]Institute for Marine and Antarctic Studies and Australian Antarctic Program Partnership, University of Tasmania, Hobart, Australia

[4]Research School of Earth Sciences, Australian National University, Canberra, Australia

[5]Australian Research Council Centre of Excellence for Climate Extremes, Australia

[6]CSIRO Oceans and Atmosphere, Hobart, Australia

[7]Application Laboratory, Japan Agency for Marine-Earth Science and Technology, Yokohama, Japan

[8]School of Mathematics and Statistics, University of New South Wales, Sydney, Australia

[9]Dpt. of Earth and Planetary Sciences, John Hopkins University, Baltimore, USA

Correspondence: L. Menviel (l.menviel@unsw.edu.au)

Abstract. While the Southern Ocean (SO) provides the largest oceanic sink of carbon, some observational studies have suggested that the total SO CO$_2$ uptake exhibited large ($\sim$0.3 GtC/yr) decadal-scale variability over the last 30 years, with a similar SO CO$_2$ uptake in 2016 than in the early 1990s. Here, using an eddy-rich ocean, sea-ice, carbon cycle model, with a nominal resolution of 1/10th degree, we explore the changes in total, natural and anthropogenic CO$_2$ fluxes in the Southern Ocean over

5 the period 1970-2021 and the processes leading to the CO$_2$ flux variability. The simulated total CO$_2$ flux exhibits decadal-scale variability with an amplitude of $\sim$0.1 GtC/yr in phase with observations and with variability in the Southern Annular Mode (SAM). Notably, a stagnation of the total CO$_2$ uptake is simulated between 1982 and 2000, while a re-invigoration is simulated between 2000 and 2012. This decadal-scale variability results from enhanced outgassing of natural CO$_2$ south of the sub-Antarctic front due to the strengthening and poleward shift of the southern hemispheric (SH) westerlies. Changes in SO

10 CO$_2$ fluxes can be mostly explained by variations in surface dissolved inorganic carbon (DIC) brought about by a combination of Ekman-driven vertical advection and DIC diffusion at the base of the mixed layer. These wind changes also lead to enhanced anthropogenic CO$_2$ uptake south of the polar front, even though the correlation is low and the amplitude 75% smaller than for the natural CO$_2$ changes. The total SO CO$_2$ uptake capability thus reduced since 1970 in response to a shift towards positive phases of the SAM. Our results indicate that, even in an eddy-rich ocean model, a strengthening and/or poleward shift of the

15 southern hemispheric westerlies enhance CO$_2$ outgassing. The projected poleward strengthening of the SH westerlies over the coming century will thus reduce the capability of the SO to mitigate the increase in atmospheric CO$_2$.

1 Introduction

As a result of anthropogenic emissions of greenhouse gases, atmospheric CO_2 concentration (CO_{2atm}) increased from a natural level of 277 ppm in 1750 (Joos and Spahni, 2008) to 415 ppm in 2021 (Friedlingstein et al., 2022). The terrestrial biosphere

20 and the ocean have however strongly mitigated the anthropogenic emissions of carbon, respectively absorbing $\sim$31% and 24% of the emissions (Le Quéré et al., 2018). The largest oceanic carbon sink is the Southern Ocean (SO), which has contributed $\sim$40% of the global oceanic CO_2 uptake in the 1990s (Sabine et al., 2004; Mikaloff-Fletcher et al., 2006). In the context of continued sustained anthropogenic emissions of greenhouse gases, a better understanding of the impact of climate change on the ocean uptake of anthropogenic CO_2 (aCO_2), but also on the total (sum of anthropogenic and natural) CO_2 (tCO_2) fluxes

25 between the ocean and the atmosphere is needed.

There is evidence for large decadal variability in the total SO carbon uptake (LeQuéré et al., 2007; Matear and Lenton, 2008; Landschützer et al., 2015; Bushinsky et al., 2019; Gruber et al., 2019b; Keppler and Landschützer, 2019). Observational estimates, covering the period 1982-2011, suggest the total carbon uptake in SO was lower than expected in the 1990s, but increased significantly between 2002 and 2011 to reach a maximum of 1.2 PgC yr^{-1} in 2011 (LeQuéré et al., 2007; Land-

30 schützer et al., 2015; Gruber et al., 2019b). Between 2011 and 2016, observational estimates suggest that the SO tCO_2 uptake weakened again (Bushinsky et al., 2019; Gruber et al., 2019b; Keppler and Landschützer, 2019). There is, however, significant uncertainty associated with these estimates due to the sparsity of the data, particularly in the 1990s (Ritter et al., 2017), and little information prior to 1982. In addition, this data scarcity might lead to a 39% overestimation of the amplitude of SO decadal tCO_2 uptake variability (Gloege et al., 2021).

35 The SO circulation is mostly driven by SH westerly winds, which generate an equatorward Ekman transport and an associated upwelling of carbon-rich deep waters. Changes in the position and strength of the SH westerlies are linked to the dominant mode of atmospheric variability in the southern hemisphere, the SAM. Positive SAM phases, which are associated with poleward contraction and stronger than average westerly winds, have been observed between 1979 and 2000, particularly during austral summer and autumn (Thompson and Solomon, 2002; Fogt and Marshall, 2020). This intensification and pole-

40 ward shift of the SH westerlies result from stratospheric ozone depletion and an increase in greenhouse gases (Arblaster and Meehl, 2006). However, due to stratospheric ozone recovery, a pause in the poleward intensification of the SH westerlies has recently been observed (Banerjee et al., 2020).

Numerical studies have highlighted the role of SH westerlies in modulating the upwelling of DIC-rich deep water and thus the carbon exchange between the atmosphere and the ocean. Stronger SH westerlies enhance the SO upwelling, leading to

45 an oceanic loss of carbon and thus an increase in CO_{2atm} (Toggweiler, 1999; Lauderdale et al., 2013; Lovenduski et al., 2007, 2008; Munday et al., 2014; Lauderdale et al., 2017; Menviel et al., 2018). The increase in surface Dissolved Inorganic Carbon (DIC) as a result of stronger SO upwelling could however be partly mitigated by enhanced export production at the surface of the SO (Menviel et al., 2008; Hauck et al., 2013). In addition, the impact of latitudinal changes in the position of the SH westerlies on oceanic carbon and CO_{2atm} is uncertain as it might depend on the initial position of the SH westerlies and

50 on how the latitudinal change in the SH westerlies impacts the oceanic circulation (Völker and Köhler, 2013; Lauderdale et al., 2013, 2017).

Most of the numerical studies analysing the impact of SH westerly changes mentioned above focused on natural carbon. Given the increase in anthropogenic carbon emissions since 1870, the natural carbon cycle has been perturbed, and the impact of changes in the strength and position of the SH westerly winds on anthropogenic carbon uptake also needs to be taken into

55 account. Only a few studies performed with coarse resolution ocean models (Lovenduski et al., 2007, 2008) have assessed the impact of the SAM on total, anthropogenic and natural CO_2 fluxes. They found that positive phases of the SAM led to an outgassing of natural CO_2 (nCO_2), while enhancing the uptake of aCO_2, with the net effect being a reduction in the tCO_2 uptake. Lenton and Matear (2007) also simulated a reduction in tCO_2 uptake in response to the SAM but did not deconvolve the natural and anthropogenic contributions.

60 Some studies have thus attributed the weaker SO carbon uptake observed in the 1990s to a positive trend in the Southern Annular Mode (SAM) (Marshall, 2003; LeQuéré et al., 2007; Lenton and Matear, 2007; Lovenduski et al., 2007, 2008). On the other hand, McKinley et al. (2020) suggested that the lower 1990s CO_2 uptake was a response to the slower CO_{2atm} growth rate. Regarding, the re-invigoration of the SO carbon uptake in the 2000s Landschützer et al. (2015) suggested that it could not be attributed to the SAM because the ERA-interim reanalysis did not display the associated wind changes. Instead,

65 they attributed the enhanced carbon uptake to increased solubility in the Pacific sector of the SO due to surface cooling, and a weaker upwelling of DIC-rich waters in the Atlantic and Indian sectors of the SO. More recently, by analysing changes in SO tCO_2 fluxes between 1980 and 2016, Keppler and Landschützer (2019) suggested that the net effect of the SAM on tCO_2 uptake was nil and that instead the variability was arising from regional shifts in surface pressure linked to zonal wavenumber 3.

70 Thus there are uncertainties not only in the decadal variability but also on the processes controlling SO carbon uptake, and there is a need for further studies examining these issues. In addition, there is a need to include the impacts of mesoscale eddy activity on the SO oceanic circulation and transport of nutrient and carbon. The prevalent mesoscale eddy activity in the SO significantly influences heat, salt and nutrient transport as well as the SO lateral and meridional overturning circulations. Mesoscale eddy transports generally act in the opposite sense to the wind driven transport in the SO, and thus the response of

75 the ocean circulation to changes in the winds varies across model studies. For example, a doubling of the magnitude of SH westerly winds doubles the simulated circumpolar transport in coarse resolution models that poorly parameterize eddies, but this doubling does not occur in eddy-resolving simulations (Hallberg and Gnanadesikan, 2006; Farneti et al., 2010; Spence et al., 2010; Dufour et al., 2012; Morrison and Hogg, 2013; Munday et al., 2013). Further, Dufour et al. (2013) showed in an eddy-permitting (∼0.5° resolution) model that even though a strengthening and poleward shift of the SH westerlies,

80 representing positive phases of the SAM, leads to stronger Ekman-induced northward natural DIC transport, a third of this is compensated by enhanced southward natural DIC transport through eddies. Dufour et al. (2013) also suggested that the higher surface DIC during positive phases of the SAM resulted from enhanced vertical diffusion at the base of the mixed layer and not from vertical advection.

Here, we analyze a simulation run over the period 1970-2021 performed with an eddy-rich ocean, sea ice, biogeochemical
85 model and forced with the 55-year Japanese Reanalysis for driving oceans (JRA55-do) (Tsujino et al., 2018) atmospheric fields
to better understand the interannual to multi-decadal variability in SO natural, anthropogenic and total CO_2 fluxes and their
links to changes in the SAM.

2   Methods

Changes in SO carbon uptake are examined using a simulation performed with the eddy-rich ACCESS-OM2-01 global model
90 configuration run under interannual forcing during 1970-2021. The ocean model is the Modular Ocean Model (MOM) version
5.1 (Griffies, 2012) with a nominal resolution of $0.1°$ and 75 vertical levels increasing smoothly in thickness from 1.1 m at the
surface to 198.4 m at the bottom (5808.7 m depth). The ocean model is coupled to the thermodynamic-dynamic Los Alamos
sea-ice model (CICE) version 5.1.2 (Hunke et al., 2017). ACCESS-OM2 is described in detail in Kiss et al. (2020), but the
version presented here has many improvements, including ocean biogeochemistry with two-way coupling to nutrient and algae
95 carried in the sea ice model (Hayashida et al., 2021).

The ocean biogeochemical model is the Nutrient-Phytoplankton-Zooplankton-Detritus (NPZD) model WOMBAT (Whole
Ocean Model of Biogeochemistry And Trophic-dynamics) (Kidston et al., 2011; Oke et al., 2013; Law et al., 2017). WOMBAT
includes DIC, $CaCO_3$, alkalinity, oxygen, phosphate and iron, that are linked to the phosphate uptake and remineralisation
through a constant Redfield ratio. The biogeochemical parameters are identical to those of the ACCESS-ESM1.5 model (Ziehn
100 et al., 2020), apart from the pre-industrial CO_{2atm} value. Two DIC tracers are included, a natural DIC (nDIC) and a total DIC
(tDIC), with the difference between the two providing an estimate of anthropogenic DIC (aDIC). nDIC exchanges carbon with a
constant pre-industrial CO_{2atm} concentration of 284.32 ppm, whereas tDIC exchanges carbon with the time evolving, observed
CO_{2atm}, which includes the current increase due to anthropogenic emissions. For the tDIC tracer, the CO_{2atm} concentration
is spatially uniform and annually-averaged, and follows the Ocean Model Intercomparison Project (OMIP) protocol until 2014
105 (Orr et al., 2017) and NOAA GML data thereafter, rising from 315.34 ppm in 1958 to 414.72 ppm in 2021, with an average
rate of increase of 1.56 ppm/yr (Fig. 2a). The air-sea CO_2 exchange is a function of wind speed (Wanninkhof, 1992) and sea ice
concentration. Note, physical and biogeochemical changes in the ocean simulations do not impact the atmospheric state, and
in all simulations the longwave radiative forcing is given by the evolving JRA55-do fields over 1970-2021. Biogeochemical
tracers also have no effect on the ocean or sea ice physical state (including shortwave penetration depth), and oxygen has no
110 effect on other biogeochemical tracers.

The model is forced by atmospheric conditions taken from the 55-year Japanese Reanalysis for driving oceans (JRA55-
do) version 1.4, 1.5.0 and 1.5.0.1 (Tsujino et al., 2018), that now covers the period 1958 to 2021. JRA55-do provides air-sea
fluxes of momentum, heat and freshwater at a 3 hourly time interval and with a horizontal resolution of $0.5625°$. The model
is forced by four 61-year cycles of JRA55-do v1.4 for the period 1958-2018. In cycle 1, the ocean model was initialised with
115 modern-day temperature and salinity distributions derived from the World Ocean Atlas 2013 version 2 (Locarnini et al., 2013).

Subsequent cycles used the final state of the previous cycle as the initial condition, and proceeded through another JRA55-do v1.4 1958-2018 forcing cycle. Cycles 1–3 do not include biogeochemistry.

Here we analyse cycle 4, which includes WOMBAT BGC and has also been extended from 2019 until the end of 2021 using JRA55-do v1.5.0 for 2019 and JRA55-do v1.5.0.1 thereafter. Ocean and ice physical fields were initialised from the values at the end of cycle 3. Biogeochemical fields other than oxygen were initialised at the start of cycle 4 (1958). A uniform 0.01 mmol m^{-3} initial value was used for phytoplankton, zooplankton, detritus and CaCO$_3$. Initial alkalinity, tDIC and nDIC were interpolated from a 305 years-long spinup run at 1 degree resolution (i.e., the first 5 cycles of OMIP2 (Mackallah et al., 2022)). GLODAPv2 (Olsen et al., 2016) was used to initialise phosphate, and iron was initialised from the FEMIP median value (Tagliabue et al., 2016). Oxygen was initialised from GLODAPv2 at 1 Jan 1979 due to a configuration mistake; this has no effect on other variables. Initial phosphate and algae in the bottom 3 cm of sea ice were set to zero, but quickly equilibrate with those in the surface ocean layer. The physical state of the ACCESS-OM2-01 global model is consistently simulated across all four, 61-year forcing cycles. Here, we skip the first twelve years of the fourth cycle (i.e. 1958-1970) from our analysis to allow the simulation to recover from the reset at the end of the previous cycle, and focus our analysis on the period 1980-2021.

In this study the SO polar front (PF) and subantarctic front (SAF) are defined as the 1.2°C annual minimum surface temperature contour, and 4°C isotherm at 400m depth, respectively following the definition of Sokolov and Rintoul (2009). Their zonal mean latitude locations are 56.3°S and 48.2°S, respectively.

To better understand the drivers of changes in ocean-atmosphere CO$_2$ fluxes, changes in natural surface water pCO$_2$ are decomposed into their nDIC, alkalinity (ALK) and solubility (sea surface salinity, SSS and sea surface temperature, SST) contributions in the following way (Sarmiento and Gruber, 2006):

$$\Delta pCO_2 = \Delta pCO_{2DIC} + \Delta pCO_{2ALK} + \Delta pCO_{2SSS} + \Delta pCO_{2SST} \tag{1}$$

The DIC, ALK and SSS contributions to ΔpCO$_2$ are of the form

$$\Delta pCO_{2X} = \gamma_X \overline{pCO_2} \Delta X / \overline{X}, \tag{2}$$

where $\overline{pCO_2}$ is the surface pCO$_2$ averaged over the years 1980-1982 and $\overline{X}$ represents the surface DIC, ALK or SSS, also averaged over 1980-1982. Here $\gamma_{DIC} = 13.3$ is the high-latitude Revelle factor, $\gamma_{ALK} = -12.6$ is the high-latitude sensitivity factor and $\gamma_{SSS} = 1$.

The SST contribution is given by

$$\Delta pCO_{2SST} = (e^{\gamma_{SST} \Delta SST} - 1) \overline{pCO_2} \tag{3}$$

where γ_{SST} is equal to 0.0423/K.

3   Results

3.1   Mean CO$_2$ flux patterns

Performances of the multi-resolution ACCESS-OM2 model suite are discussed in Kiss et al. (2020). The eddy-rich ACCESS-OM2-01 model at 0.1° resolution provides a reasonable and consistent representation of the state of the ocean, with a particularly good representation of the oceanic circulation structure, dense shelf water formation and abyssal overturning cell (Morrison et al., 2020). The simulated horizontal and vertical gradients in tDIC, alkalinity and dissolved oxygen (O$_2$) in the Southern Ocean are in good agreement with observations (Olsen et al., 2016) (Fig. S1). The absolute values of tDIC and alkalinity are ∼60 μmol/kg^{-1} lower than those estimated by GLODAP. This bias might lead to a ∼ 10-15 ppm underestimation of the total pCO$_2$ of SO waters, which can explain the slight overestimation of the SO tCO$_2$ uptake as detailed below.

The mean SO tCO$_2$, nCO$_2$ and aCO$_2$ fluxes averaged over years 1982-2021 are shown in figure 1. tCO$_2$ fluxes can be compared to observational estimates derived from the self-organizing map-feed-forward neural network (SOM-FFN) dataset (Landschützer et al., 2015) and from autonomous biogeochemical floats (Gray et al., 2018; Prend et al., 2022). When averaged over years 1982-2021, the SO is a net sink of tCO$_2$ with a strong uptake simulated north of the SAF (Sokolov and Rintoul, 2009), in agreement with observations. Some areas however display an outgassing of tCO$_2$, mostly south of the PF, but also between the SAF and the PF in parts of the Atlantic and Indian sectors. Observational estimates also suggest moderate outgassing south of the PF. Overall, the average SO tCO$_2$ uptake is 0.37 GtC/yr higher in the simulation than the observational estimates. When zonally integrated, tCO$_2$ fluxes are small south of 50°S and the ocean uptake peaks at about 40°S (Fig. S2e).

These fluxes can be decomposed into their nCO$_2$ and aCO$_2$ components, thus highlighting an uptake of aCO$_2$ everywhere south of 35°S (Fig. 1d), with a maximum south of the PF (∼56.3°S, Fig. S2d). By contrast, an outgassing of nCO$_2$ is simulated south of the PF and in the frontal zone of the Indian sector (Fig. 1c). While the simulated nCO$_2$ outgassing is very localized during 1980-1984, it is in the order of 0.1 x 10^8 molC/m/yr since the late 1990s (Fig. S2c).

The upwelling of DIC-rich deep waters south of the PF (Figs. 1e and S2b) and the subsequent northward advection of these waters contribute to the nCO$_2$ outgassing south of 50°S. Through Ekman transport, surface waters in the SO move equatorward, and nutrients and DIC are consumed by phytoplankton, leading to nCO$_2$ ocean uptake north of the SAF, where Antarctic Intermediate Waters (AAIW) and Subantarctic Mode Waters (SAMW) are formed.

3.2   Temporal changes in CO$_2$ fluxes

We now look at the time evolution of SO CO$_2$ fluxes since 1970 (Fig. 2). From 1970 to 2021, the SO nCO$_2$ uptake (Fig. 2c) reduces by ∼0.25 GtC/yr (mean slope of 0.05 GtC/yr per decade). The nCO$_2$ uptake is stronger than the 1970-2021 mean before the mid-1990s and weaker after that. On top of the long-term trend, the nCO$_2$ flux displays a large (∼0.15 GtC/yr) decadal-scale variability. nCO$_2$ fluxes are strongly correlated with the SAM index calculated from the JRA-55do dataset (R=0.62 for annual mean data and R=0.82 with a 5-year smoothing, Figs. 2b and S3), with periods of weak nCO$_2$ uptake associated with positive phases of the SAM. While this is compared to the SAM index calculated from the JRA-55do dataset (Stewart et al., 2020), similar correlations are found with the observed SAM index (Marshall, 2003). This SAM link is largely related to changes in

the strength of the zonal SO wind stress (Fig. S3, R=0.6 for yearly data, 0.8 with 5-year smoothing), even though a poleward displacement of the maximum wind stress also reduces the nCO_2 uptake (Fig. S3, R=-0.46). The nCO_2 outgassing occurs in the SO upwelling area (south of 55°S), but also up to 50°S due to the northward advection DIC-rich waters (Fig. 1c,e).

180 The simulated aCO_2 uptake increases by 0.8 GtC/yr over the period 1970-2021 (Fig. 2d) noting that the CO_{2atm} growth rate, which is a forcing of the model, also increases by 2 ppm/yr during that time (Fig. 2a). To better highlight variability in the aCO_2 flux, we detrend it and plot the anomaly with respect to the 1970-2021 mean (Fig. 2e). The aCO_2 uptake also features decadal-scale variability, but with an amplitude that is about 30% lower than for nCO_2. A weak relationship between aCO_2 uptake and the SAM is simulated (R=-0.29, Fig. S3). This weak association is mostly due to the impact of stronger wind stress

185 (R=0.24, Fig. S3). The increase in aCO_2 uptake occurs everywhere south of 35°S, but particularly south of 50°S (Fig. S2d).

  The combined effect of reduced nCO_2 uptake, increased aCO_2 uptake (mostly due to the increase in CO_{2atm}) lead to a 0.55 GtC/yr increase in tCO_2 uptake between 1970 and 2021 (Fig. 2f). The tCO_2 uptake also features decadal-scale variability, with a stagnation of tCO_2 uptake between 1982 and 2000, a reinvigoration in the early 2000s and only ∼0.1 GtC/yr increase since 2010. The simulated tCO_2 fluxes can be compared to the observational estimates derived from the SOM-FFN and based

190 on the Surface Ocean CO2 Atlas Database (SOCAT) and Southern Ocean Carbon and Climate Observations and Modeling (SOCCOM) biogeochemistry floats from 1982 to 2017 (Landschützer et al., 2019; Bushinsky et al., 2019) (Fig. 2h). The simulated and observational estimates of tCO_2 flux are well correlated (R=0.55) and both display minimum tCO_2 uptake in 2000-2001, and maximum in the early 1990s and early 2010s. While the simulated amplitude of the variations is about half of the observed one, it is within the uncertainty range of the observational estimate (±0.25 GtC/yr) (Bushinsky et al., 2019).

195 Since changes in tCO_2 flux are also impacted by the CO_{2atm} increase, we detrend the SO tCO_2 flux and plot the anomaly with respect to the detrended 1970-2021 mean to properly assess the decadal-scale variability (Fig. 2g). The detrended tCO_2 flux thus presents variations similar to nCO_2, with reduced total uptake during positive phases of the SAM. The nCO_2 flux variability dominates the changes in tCO_2 uptake with a strengthening of the winds and a poleward shift both reducing the tCO_2 uptake (Figs. 2c,g and S3).

200 3.3 Processes leading to changes in natural CO_2 fluxes

To better understand the changes in nCO_2 flux we calculate the changes in surface natural pCO_2 arising from thermal and non-thermal (sum of nDIC, alkalinity and salinity) contributions in the different sectors of the Southern Ocean (Fig. 3). As the outgassing of nCO_2 occurs south of the SAF, we focus our analysis on that region. The natural pCO_2 increase south of 50°S since the 1990s is due to non-thermal contributions. Given that the surface salinity changes are negligible, this increase

205 is thus due to higher surface nDIC, partly compensated by an increase in surface alkalinity. Changes in SST oppose the non-thermal pCO_2 changes, with a decrease in SST during positive phases of the SAM. The non-thermal pCO_2 evolution, which closely follows the nCO_2 fluxes (Fig. S4), differs in each sector. In particular, natural pCO_2 variations in the Pacific sector are significant throughout the period but do not display a clear trend. On the other hand, the Indian and Atlantic pCO_2 variations are negligible until the mid to late 1990s but match the Pacific contribution in 2015/2016. These changes in natural pCO_2, and

210 thus nCO_2 fluxes impact the tCO_2 fluxes, with lower tCO_2 uptake in the Pacific basin in the late 1990s compared to the other

basins, whereas the Pacific tCO$_2$ uptake is higher in the Pacific than in the other basins in the 2010s (Fig. S4), in agreement
with observations (Keppler and Landschützer, 2019).

The non-thermal pCO$_2$ changes are significantly correlated with changes in the strength of the westerlies in each sector of the
Southern Ocean (Fig. 3). The inter-basin differences in SH westerlies latitudinal trends probably contributed to the relatively
215 larger increase in surface natural pCO$_2$ in the Atlantic and Indian sectors compared to the Pacific sector. Indeed, in the JRA55-
do dataset there is a ∼1.5° and ∼1° poleward shift in the Atlantic and Indian sectors, respectively starting in the late 1990s,
while there are no significant latitudinal changes in the Pacific sector (Fig. S5). This is broadly consistent with observations,
which suggest a ∼1° poleward shift in the Atlantic and Indian sector and a ∼1° equatorward shift in the Pacific sector since
the 1980s (Waugh et al., 2020).

220 Overall, an increase in surface natural pCO$_2$ is simulated as a response to an increase in surface nDIC, with a small contri-
bution from an increase in SST since the late 2010s. Superimposed on this trend are increases in pCO$_2$ driven by higher nDIC
during positive phases of the SAM. To better highlight the quantitative impact of positive phases of the SAM, we perform a
composite of the years in which the annual mean SAM index as calculated from the JRA55-do dataset was greater than 0.83
(i.e. 1998, 1999, 2010, 2015 and 2021) and compare this to a composite of negative SAM years (SAM index≤-0.33: 1980,
225 1991, 1992, 2002).

During these strong positive phases of the SAM, a significant increase (≥1 mol/m^2/yr) in nCO$_2$ outgassing is simulated south
of the PF (Fig. 4a). Some enhanced nCO$_2$ outgassing is also simulated between the SAF and PF in the Indian and southwest
Pacific sector as well as north of the SAF in the Pacific sector. This nCO$_2$ outgassing mostly results from an increase in surface
nDIC concentration (Fig. 4b, 6b).

230 The stronger and poleward shifted westerlies during positive phases of the SAM enhance the Ekman-driven vertical DIC
advection south of the PF (Figs. 4g and 5b). The associated deepening of the mixed layer also drives an increase in vertical
DIC diffusion at the base of the mixed layer (Figs. 4e,f and 5c). South of the PF, the Ekman-driven vertical DIC advection and
vertical diffusion at the base of the mixed layer contribute equally to the DIC increase (2.8 GtC/yr). The eddy-driven vertical
DIC advection (taken as the difference between the vertical DIC advection and the Ekman-driven vertical DIC advection)
235 further contributes to the higher surface DIC south of 60°S (+0.7 GtC/yr, not shown). However, north of the PF, the Ekman-
driven vertical DIC advection decreases surface DIC, while vertical diffusion at the base of the mixed layer leads to a DIC
increase in the mixed layer. In this simulation, changes in biological export of carbon are two order of magnitude smaller than
the Ekman-driven and vertical diffusion contributions and therefore do not affect significantly changes in nCO$_2$ fluxes (Fig.
5d).

240 Due to the long-term shift towards positive phases of the SAM, the composite of positive SAM is shifted towards more
recent years than the composite of negative phases. If we correct for this (i.e. assuming that the aCO$_2$ uptake follows a linear
trend), then an anomalous aCO$_2$ uptake is simulated south of PF (Fig. 4c), in regions where a stronger nCO$_2$ outgassing is
simulated (Fig. 4a). The amplitude of the aCO$_2$ anomalies are however only equivalent to ∼25% of the nCO$_2$ anomalies (Figs.
4 5f black line). As a result, reduced tCO$_2$ uptake is simulated south of the PF during positive phases of the SAM (Fig. S6). If a

245 similar correction is applied to compensate for the difference in mean year between the positive and negative SAM composites, then an anomalous tCO_2 outgassing is simulated almost everywhere in the SO (Figs. 4d and 5g, black line).

It is interesting to note that south of the PF, the structure of the mean nCO_2 and aCO_2 fluxes averaged over the period 1981-2021 (Fig. 1) are similar to the anomalies obtained for positive phases of the SAM (Fig. 4), indicating that the positive phases of the SAM simply accentuate the mean SO features (i.e. nCO_2 outgassing gets stronger in outgassing regions). This is 250 however not the case north of the SAF in the Pacific sector, where the nCO_2 uptake is reduced during positive phases of the SAM.

Some of the main areas of nCO_2 outgassing and aCO_2 uptake correspond to major topographic features of the SO: namely, the eastern part of the Southeast Indian Ridge, the Drake Passage and the Southwest Indian Ridge (Fig. 1e). On the contrary, the cyclonic circulation in the relatively deep part of the Ross Sea is associated with nCO_2 uptake. This could be due to enhanced 255 eddy mixing over topography linked to the merging of multiple jets (Lu and Speer, 2010), and warrants further study.

3.4 Changes in oceanic DIC

We now look into the changes in oceanic natural, anthropogenic and total DIC concentration between 1980 and 2021 in the different sectors of the Southern Ocean. As discussed above, the outgassing of natural carbon in the SO increases with wind stress as the upwelling of DIC-rich waters and vertical diffusion at the base of the mixed layer are enhanced. An increase 260 in nDIC is simulated within the upper Circumpolar Deep Water (CDW), particularly in the Pacific sector and somewhat in the Indian sector (Fig. 7d-f). This increase is linked to higher nDIC within the Indian and Pacific deep waters (IDW and PDW, respectively). Higher nDIC is also simulated within the upwelling branch of the North Atlantic Deep Water in the Atlantic sector. These nDIC increases are associated with negative dissolved oxygen (O_2) anomalies (Fig. 7a-c) and are due to an increase in remineralized DIC (Fig. S7), thus indicating a higher proportion of older/deeper waters. On the other hand, 265 a decrease in nDIC is simulated within the SAMW, the lower CDW, and within AABW. The negative nDIC anomalies at depth are mostly visible in the Atlantic and Indian sectors as the anomalies are concentrated in the AABW formation regions (Weddell Sea, Ross Sea and Adelie coast), and their subsequent transport westward around Antarctica (Morrison et al., 2020; Solodoch et al., 2022). The negative nDIC anomalies are due to reduced remineralized DIC content and are associated with positive O_2 anomalies. This implies either reduced nutrient utilisation in the Southern Ocean and/or higher transport rates of 270 SAMW and AABW.

The strengthening and poleward shift of the SH westerlies since 1980 also impacts the nDIC distribution within the SO with a reduced vertical gradient south of the SAF, linked to a reduction in regenerated carbon at depth. This weaker biological pump efficiency in 2017-2021 compared to 1980-1982 could result from the lower residence time in the SO, arising from the higher SO upwelling rate and potentially higher mixing at depth due to the poleward intensified westerlies, and associated changes in 275 windstress curl (Fig. S2).

We next look at the evolution of nDIC in the subsurface of the SO between 1980 and 2021, and assess its link to the surface variability (Fig. 8). The nDIC concentration at 1000m depth gradually increases at all latitudes during that time period, but with a steepest increase between 45°S and 60°S, which corresponds to the upwelling branch of the IPW, PDW and NADW. At

400m depth, nDIC also increases south of the SAF due to the enhanced upwelling of nDIC-rich deep waters. On the other hand, nDIC at 400m depth decreases north of the SAF within SAMW. This contrasting behavior north and south of the SAF could be linked to the poleward shift of the SH westerlies. At both 400m and 1000m depth, decadal-scale DIC variations are visible. The fast response of subsurface DIC to the surface forcing is consistent with nDIC changes being due to Ekman pumping and associated isopycnal displacement, which respond quickly to surface forcing (Waugh and Haine, 2020).

In the simulation presented here, the Southern Ocean absorbs 27 Gt of anthropogenic carbon between 1970 and 2021. In the SO, the highest increase is within AAIW and SAMW, in agreement with observations (Gruber et al., 2019a) (Fig. S8). A minor part of anthropogenic DIC (aDIC) is also entrained within AABW. As expected due to relative water-mass ventilation rates, the smallest increase in aDIC is simulated within the upper CDW of the Pacific basin, while relatively large ($\geq$5 mmol/m^3) increases in aDIC can be seen close to the Antarctic shelf in the Indian sector between 1980 and 2021. This could be linked to the deepening of the mixed layer depth off the Adelie coast in the model runs.

If we assume a linear increase in oceanic aDIC based on the simulated accumulation in the 1970s (Gruber et al., 2019a), then the anomalous aDIC concentration is high (≥ 5 mmol/m^3) within AAIW and SAMW as well as within the upper 500 m on the Antarctic shelf (Fig. 7g-i), indicating enhanced entrainment of aDIC within these water-masses and potentially AABW. Small negative aDIC anomalies are however simulated within the upwelling branch of IDW, and to a lesser extent NADW and PDW. These correspond to regions with positive nDIC and remineralized DIC anomalies as well as negative O_2 anomalies, thus confirming the increased proportion of older, DIC-rich deep waters.

As a result the corrected total DIC (from which the linear aDIC increase has been removed) increases within SAMW, AAIW and the upper CDW by 19 mmol/m^3, 11 mmol/m^3 and 3 mmol/m^3, respectively, while there are little changes below 2000 m depth, or even small negative anomalies in the deep Atlantic and Indian Oceans (Fig. 7j-l). This indicates a reduction in the vertical tDIC gradient in the Southern Ocean.

4 Discussion and conclusions

We have used an eddy-rich global ocean, sea-ice, carbon cycle model to assess changes in SO total, natural and anthropogenic CO_2 fluxes over the last 50 years. The multi-decadal strengthening and poleward shift of the SH westerlies, associated with a shift towards positive phases of the SAM during that period, drives a decrease in nCO_2 uptake with a trend of -0.007 GtC/yr^2. On the other hand, the increase in CO_{2atm} growth rate leads to a higher aCO_2 uptake with a trend of 0.014 PgC/yr^2. The results presented here suggest that the strengthening and poleward shift of the SH westerlies only had a small impact on aCO_2 uptake. As a result, while the tCO_2 uptake increases between 1980 and 2021 with a trend of 0.007 PgC/yr^2, it would have likely increased twice as fast without a strengthening and poleward shift of the SH westerlies. These CO_2 flux trends simulated with a high-resolution eddy-rich model are consistent with those of Lovenduski et al. (2008), who simulated an increase in nCO_2 outgassing between 1979 and 2004 with a trend of 0.004 PgC/yr^2, an increase in aCO_2 uptake with a trend of 0.011 PgC/yr^2 and thus an increase in tCO_2 uptake of 0.007 PgC/yr^2 using a coarse resolution ocean model. The multi-decadal, large-scale

oceanic carbon cycle response to a strengthening and poleward shift of the SH westerlies is thus robust from eddy-rich to coarse resolution models.

In addition, the total air-sea CO_2 fluxes exhibit large (∼0.1 GtC/yr) decadal-scale variability thus supporting previous inferences of decadal scale changes in SO CO_2 fluxes (Li and Ilyina, 2018; Lovenduski et al., 2008; Landschützer et al., 2015;

315 Gruber et al., 2019b). The simulated variability is not as large as that derived from observational estimates (Landschützer et al., 2016; Bushinsky et al., 2019; Keppler and Landschützer, 2019), but is within the uncertainty band (Gruber et al., 2019b; Bushinsky et al., 2019). Such a mismatch between simulated SO tCO_2 variations and observations is prevalent in hindcast simulations (Gruber et al., 2019b). It should be noted that it has been suggested that the observed SO CO_2 flux variability could be overestimated (Gloege et al., 2021). In addition, the underestimation of the simulated tCO_2 uptake in the late 2000s/early

320 2010s could be due a mis-representation of Southern Ocean stratification. It has indeed been suggested that the overturning rate of the lower cell was weaker during that time period (DeVries et al., 2017) due to enhanced stratification in the Southern Ocean (de Lavergne et al., 2014), linked to enhanced Antarctic basal melt rates (Adusumilli et al., 2020).

To first order, the simulated decadal scale changes in tCO_2 fluxes are due to changes in nCO_2 fluxes primarily arising from changes in the magnitude of the SH westerlies, but also due to variations in the latitudinal position of the SH winds. While

325 we find a strong link between regional wind changes and nCO_2/tCO_2 fluxes, we find that minima in tCO_2 uptake arise from a strengthening and/or poleward shift of the SH westerlies, and thus positive phases of the SAM.

A stagnation of SO tCO_2 uptake between 1980 and 2000 is simulated. This time period corresponds to the largest rate of westerly wind stress increase, but also a poleward shift of the westerlies. The timing and magnitude of this stagnation in tCO_2 uptake in the SO is in agreement with observational estimates (Lovenduski et al., 2008; Landschützer et al., 2015; Gruber

330 et al., 2019b; Keppler and Landschützer, 2019). While the impact of the SAM on SO CO_2 fluxes is clear in our simulation, the early 1990s also feature the lowest atmospheric CO_2 growth rate of the period studied here (McKinley et al., 2020). The simulated SO aCO_2 uptake in the early 1990s is thus the lowest of the period, noting that positive phases of the SAM are usually associated with slightly enhanced aCO_2 uptake. Our results thus also support the conclusion that the slowdown of the SO tCO_2 uptake in the early 1990s was due to a low atmospheric CO_2 growth rate (McKinley et al., 2020) and not a positive

335 phase of the SAM (LeQuéré et al., 2007; Lovenduski et al., 2008; Matear and Lenton, 2008). In agreement with observations, a re-invigoration of tCO_2 uptake is simulated in the early 2000s (Keppler and Landschützer, 2019), mostly due to a pause in the positive SAM trend. Since the mid 2000s, the tCO_2 uptake has increased slowly, but we find that the reversal in tCO_2 uptake that had been highlighted in the mid 2010s (Keppler and Landschützer, 2019) was short-lived and due to the strong positive 2015 SAM.

340 The enhanced nCO_2 outgassing during positive phases of the SAM is due to higher surface nDIC concentration south of the PF, partly compensated by lower SST. This increase in surface nDIC results from enhanced vertical nDIC advection, mostly Ekman driven, as well as enhanced vertical nDIC diffusion at the base of the mixed layer. This significant role of vertical diffusion is in agreement with a previous study performed with an eddy-permitting model (Dufour et al., 2013), even if contrarily to that study we find an equal weight of vertical advection and Ekman pumping south of the PF. As in previous

345 studies, we find that biological processes do not significantly impact air-sea CO_2 fluxes on decadal-time scales, and that the changes in surface nDIC arise from changes in oceanic circulation (Dufour et al., 2013).

Previous studies have suggested that wind-driven changes in oceanic circulation in the Southern Ocean are partially compensated by the eddy-driven transport (Morrison and Hogg, 2013). Similarly, Dufour et al. (2013) suggested that 1/3 of the Ekman-driven DIC transport arising from positive phases of the SAM was compensated by eddy transport. Here, despite a 20%

350 increase in wind stress, only a small ACC increase (134 to 138 Sv) is simulated thus supporting the eddy saturation theory. Yet, we find that changes in the position and strength of the SH westerlies lead to an outgassing of nCO_2 on a yearly as well as multi-decadal timescale, with an amplitude similar to that found in previous studies performed with coarser resolution models (Dufour et al., 2013; Lovenduski et al., 2007). This is an important result as it was suggested that mesoscale eddies would compensate for the wind-driven circulation in the Southern Ocean, thus mitigating the carbon cycle response to changes in the

355 strength and position of the westerlies. Here we show that even in an eddy-rich model, a strengthening and/or a poleward shift of the westerlies leads to enhanced CO_2 outgassing.

If SH westerly winds continue to strengthen, as projected under RCP8.5/SSP5-85 scenarios (Grose et al., 2020; Goyal et al., 2021), our experiments suggest that the increase in aCO_2 uptake would be partly compensated by nCO_2 outgassing, thus only leading to a small increase in tCO_2 uptake. Future changes in SO carbon uptake will thus likely result from a fine balance

360 between natural carbon release and anthropogenic carbon uptake, which will itself depend on changes in SH westerlies, SO stratification and temperature as well as the rate of anthropogenic carbon emissions.

Acknowledgements. This project was supported by the Australian Research Council (ARC), including grants FT180100606, FT190100413, and SR200100008 AEK was supported by ARC grants LP160100073 and LP200100406, and the Australian Government's Australian Antarctic Science Program grant 4541.

365 The authors thank the Consortium for Ocean-Sea Ice Modelling in Australia (COSIMA; http://www.cosima.org.au) for making the ACCESS-OM2 suite of models available at https://github.com/COSIMA/access-om2. Model runs were undertaken with the assistance of resources from the National Computational Infrastructure (NCI), which is supported by the Australian Government.

Data availability The modelling outputs presented here have been deposited on UNSWorks (https://unsw-primo.hosted.exlibrisgroup.com/primo-explore/search?vid=UNSWORKS). A doi will be generated upon accep-
370 tance of the manuscript.

References

Adusumilli, S., Fricker, H., Medley, B., Padman, L., and Siegfried, M.: Interannual variations in meltwater input to the Southern Ocean from Antarctic ice shelves, Nature Geosciences, 13, 616–620, https://doi.org/10.1038/s41561-020-0616-z, 2020.

Arblaster, J. M. and Meehl, G. A.: Contributions of External Forcings to Southern Annular Mode Trends, Journal of Climate, 19, 2896–2905,
375 https://doi.org/10.1175/JCLI3774.1, 2006.

Banerjee, A., Fyfe, J., Polvani, L., Waugh, D., and Chang, K.-L.: A pause in Southern Hemisphere circulation trends due to the Montreal Protocol, Nature, 579, 544–548, https://doi.org/10.1038/s41586-020-2120-4, 2020.

Bushinsky, S. M., Landschützer, P., Rödenbeck, C., Gray, A. R., Baker, D., Mazloff, M. R., Resplandy, L., Johnson, K. S., and Sarmiento, J. L.: Reassessing Southern Ocean Air-Sea CO2 Flux Estimates With the Addition of Biogeochemical Float Observations, Global Bio-
380 geochemical Cycles, 33, 1370–1388, https://doi.org/https://doi.org/10.1029/2019GB006176, 2019.

de Lavergne, C., Palter, J., Galbraith, E., Bernardello, R., and Marinov, I.: Cessation of deep convection in the open Southern Ocean under anthropogenic climate change, Nature Climate Change, 4, 278–282, https://doi.org/10.1038/NCLIMATE2132, 2014.

DeVries, T., Holzer, M., and Primeau, F.: Recent increase in oceanic carbon uptake driven by weaker upper-ocean overturning, Nature, 542, 215–218, https://doi.org/10.1038/nature21068, 2017.

385 Dufour, C. O., Sommer, J. L., Zika, J., Gehlen, M., Orr, J., Mathiot, J., and Barnier, B.: Standing and Transient Eddies in the Response of the Southern Ocean Merid- ional Overturning to the Southern Annular Mode, J. Climate, 25, 6958–6974, 2012.

Dufour, C. O., Sommer, J. L., Gehlen, M., Orr, J. C., Molines, J.-M., Simeon, J., and Barnier, B.: Eddy compensation and controls of the enhanced sea-to-air CO2 flux during positive phases of the Southern Annular Mode, Global Biogeochemical Cycles, 27, 950–961, https://doi.org/10.1002/gbc.20090, 2013.

390 Farneti, R., Delworth, T., Rosati, A., Griffies, S., and Zeng, F.: The role of mesoscale eddies in the rectification of the Southern Ocean response to climate change, J. Phys. Oceanogr., 40, 1539–1557, 2010.

Fogt, R. L. and Marshall, G. J.: The Southern Annular Mode: Variability, trends, and climate impacts across the Southern Hemisphere, WIREs Climate Change, 11, e652, https://doi.org/10.1002/wcc.652, 2020.

Friedlingstein, P., Jones, M. W., O'Sullivan, M., Andrew, R. M., Bakker, D. C. E., Hauck, J., Le Quéré, C., Peters, G. P., Peters, W., Pongratz,
395 J., Sitch, S., Canadell, J. G., Ciais, P., Jackson, R. B., Alin, S. R., Anthoni, P., Bates, N. R., Becker, M., Bellouin, N., Bopp, L., Chau, T. T. T., Chevallier, F., Chini, L. P., Cronin, M., Currie, K. I., Decharme, B., Djeutchouang, L. M., Dou, X., Evans, W., Feely, R. A., Feng, L., Gasser, T., Gilfillan, D., Gkritzalis, T., Grassi, G., Gregor, L., Gruber, N., Gürses, O., Harris, I., Houghton, R. A., Hurtt, G. C., Iida, Y., Ilyina, T., Luijkx, I. T., Jain, A., Jones, S. D., Kato, E., Kennedy, D., Klein Goldewijk, K., Knauer, J., Korsbakken, J. I., Körtzinger, A., Landschützer, P., Lauvset, S. K., Lefèvre, N., Lienert, S., Liu, J., Marland, G., McGuire, P. C., Melton, J. R., Munro, D. R., Nabel,
400 J. E. M. S., Nakaoka, S.-I., Niwa, Y., Ono, T., Pierrot, D., Poulter, B., Rehder, G., Resplandy, L., Robertson, E., Rödenbeck, C., Rosan, T. M., Schwinger, J., Schwingshackl, C., Séférian, R., Sutton, A. J., Sweeney, C., Tanhua, T., Tans, P. P., Tian, H., Tilbrook, B., Tubiello, F., van der Werf, G. R., Vuichard, N., Wada, C., Wanninkhof, R., Watson, A. J., Willis, D., Wiltshire, A. J., Yuan, W., Yue, C., Yue, X., Zaehle, S., and Zeng, J.: Global Carbon Budget 2021, Earth System Science Data, 14, 1917–2005, https://doi.org/10.5194/essd-14-1917-2022, 2022.

405 Gloege, L., McKinley, G. A., Landschützer, P., Fay, A. R., Frölicher, T. L., Fyfe, J. C., Ilyina, T., Jones, S., Lovenduski, N. S., Rodgers, K. B., Schlunegger, S., and Takano, Y.: Quantifying Errors in Observationally Based Estimates of Ocean Carbon Sink Variability, Global Biogeochemical Cycles, 35, e2020GB006 788, https://doi.org/10.1029/2020GB006788, 2021.

Goyal, R., Sen Gupta, A., Jucker, M., and England, M. H.: Historical and Projected Changes in the Southern Hemisphere Surface Westerlies, Geophysical Research Letters, 48, e2020GL090 849, https://doi.org/https://doi.org/10.1029/2020GL090849, 2021.

410 Gray, A. R., Johnson, K. S., Bushinsky, S. M., Riser, S. C., Russell, J. L., Talley, L. D., Wanninkhof, R., Williams, N. L., and Sarmiento, J. L.: Autonomous Biogeochemical Floats Detect Significant Carbon Dioxide Outgassing in the High-Latitude Southern Ocean, Geophysical Research Letters, 45, 9049–9057, https://doi.org/10.1029/2018GL078013, 2018.

Griffies, S.: Elements of the Modular Ocean Model (MOM): 2012 release (GFDL Ocean Group Technical Report No. 7), Tech. rep., NOAA/-Geophysical Fluid Dynamics Laboratory, Princeton, USA, 2012.

415 Grose, M. R., Narsey, S., Delage, F. P., Dowdy, A. J., Bador, M., Boschat, G., Chung, C., Kajtar, J. B., Rauniyar, S., Freund, M. B., Lyu, K., Rashid, H., Zhang, X., Wales, S., Trenham, C., Holbrook, N. J., Cowan, T., Alexander, L., Arblaster, J. M., and Power, S.: Insights From CMIP6 for Australia's Future Climate, Earth's Future, 8, e2019EF001 469, https://doi.org/10.1029/2019EF001469, 2020.

Gruber, N., Clement, D., Carter, B. R., Feely, R. A., van Heuven, S., Hoppema, M., Ishii, M., Key, R. M., Kozyr, A., Lauvset, S. K., Lo Monaco, C., Mathis, J. T., Murata, A., Olsen, A., Perez, F. F., Sabine, C. L., Tanhua, T., and Wanninkhof, R.: The oceanic sink for
420 anthropogenic CO2 from 1994 to 2007, Science, 363, 1193–1199, https://doi.org/10.1126/science.aau5153, 2019a.

Gruber, N., Landschützer, P., and Lovenduski, N.: The variable Southern Ocean carbon sink, Annual Review of Marine Science, 11, 159–186, 2019b.

Hallberg, R. and Gnanadesikan, A.: The role of eddies in determining the structure and response of the wind-driven southern hemisphere overturning : Results from the modeling eddies in the Southern Ocean (MESO) project, Journal of Physical Oceanography, 36, 2232–2252,
425 2006.

Hauck, J., Völker, C., Wang, T., Hoppema, M., Losch, M., and Wolf-Gladrow, D. A.: Seasonally different carbon flux changes in the Southern Ocean in response to the southern annular mode, Global Biogeochemical Cycles, 27, 1236–1245, https://doi.org/10.1002/2013GB004600, 2013.

Hayashida, H., Jin, M., Steiner, N. S., Swart, N. C., Watanabe, E., Fiedler, R., Hogg, A. M., Kiss, A. E., Matear, R. J., and Strutton, P. G.: Ice
430 Algae Model Intercomparison Project phase 2 (IAMIP2), Geoscientific Model Development, 14, 6847–6861, https://doi.org/10.5194/gmd-14-6847-2021, 2021.

Hunke, E., Lipscomb, W., Jones, P., Turner, A., Jeffery, N., and Elliott, S.: CICE, The Los Alamos Sea Ice Model, Version 00, https://doi.org/https://www.osti.gov/biblio/1364126, 2017.

Joos, F. and Spahni, R.: Rates of change in natural and anthropogenic radiative forcing over the past 20,000 years, Proceedings of the National
435 Academy of Sciences, 105, 1425–1430, https://doi.org/10.1073/pnas.0707386105, 2008.

Keppler, L. and Landschützer, P.: Regional Wind Variability Modulates the Southern Ocean Carbon Sink, Sci. Rep., 7384, https://doi.org/10.1038/s41598-019-43826-y, 2019.

Kidston, M., Matear, R., and Baird, M.: Parameter optimisation of a marine ecosystem model at two contrasting stations in the Sub-Antarctic Zone, Deep-Sea Research II, 58, 2301–2315, 2011.

440 Kiss, A. E., Hogg, A. M., Hannah, N., Boeira Dias, F., Brassington, G. B., Chamberlain, M. A., Chapman, C., Dobrohotoff, P., Domingues, C. M., Duran, E. R., England, M. H., Fiedler, R., Griffies, S. M., Heerdegen, A., Heil, P., Holmes, R. M., Klocker, A., Marsland, S. J., Morrison, A. K., Munroe, J., Nikurashin, M., Oke, P. R., Pilo, G. S., Richet, O., Savita, A., Spence, P., Stewart, K. D., Ward, M. L., Wu, F., and Zhang, X.: ACCESS-OM2 v1.0: a global ocean–sea ice model at three resolutions, Geoscientific Model Development, 13, 401–442, https://doi.org/10.5194/gmd-13-401-2020, 2020.

445 Landschützer, P., Gruber, N., Haumann, F. A., Rödenbeck, C., Bakker, D. C. E., van Heuven, S., Hoppema, M., Metzl, N., Sweeney, C., Takahashi, T., Tilbrook, B., and Wanninkhof, R.: The reinvigoration of the Southern Ocean carbon sink, Science, 349, 1221–1224, https://doi.org/10.1126/science.aab2620, 2015.

Landschützer, P., Gruber, N., and Bakker, D. C. E.: Decadal variations and trends of the global ocean carbon sink, Global Biogeochemical Cycles, 30, https://doi.org/10.1002/2015GB005359, 2016.

450 Landschützer, P., Bushinsky, S. M., and Gray, A. R.: A combined globally mapped CO_2 flux estimate based on the Surface Ocean CO2 Atlas Database (SOCAT) and Southern Ocean Carbon and Climate Observations and Modeling (SOCCOM) biogeochemistry floats from 1982 to 2017, Dataset, NOAA National Centers for Environmental Information, https://doi.org/10.25921/9hsn-xq82, 2019.

Lauderdale, J. M., Garabato, A. C. N., Oliver, K. I. C., Follows, M. J., and Williams, R. G.: Wind-driven changes in Southern Ocean residual circulation, ocean carbon reservoirs and atmospheric CO_2, Climate Dynamics, 41, 2145–2164, https://doi.org/10.1007/s00382-012-1650-3, 2013.

455 Lauderdale, J. M., Williams, R. G., Munday, D. R., and Marshall, D. P.: The impact of Southern Ocean residual upwelling on atmospheric CO2 on centennial and millennial timescales, Climate Dynamics, 48, 1611–1631, https://doi.org/10.1007/s00382-016-3163-y, 2017.

Law, R. M., Ziehn, T., Matear, R. J., Lenton, A., Chamberlain, M. A., Stevens, L. E., Wang, Y. P., Srbinovsky, J., Bi, D., Yan, H., and Vohralik, P. F.: The carbon cycle in the Australian Community Climate and Earth System Simulator (ACCESS-ESM1) – Part 1: Model description
460 and pre-industrial simulation, Geoscientific Model Development, 10, 2567–2590, https://doi.org/10.5194/gmd-10-2567-2017, 2017.

Le Quéré, C., Andrew, R. M., Friedlingstein, P., Sitch, S., Pongratz, J., Manning, A. C., Korsbakken, J. I., Peters, G. P., Canadell, J. G., Jackson, R. B., Boden, T. A., Tans, P. P., Andrews, O. D., Arora, V. K., Bakker, D. C. E., Barbero, L., Becker, M., Betts, R. A., Bopp, L., Chevallier, F., Chini, L. P., Ciais, P., Cosca, C. E., Cross, J., Currie, K., Gasser, T., Harris, I., Hauck, J., Haverd, V., Houghton, R. A., Hunt, C. W., Hurtt, G., Ilyina, T., Jain, A. K., Kato, E., Kautz, M., Keeling, R. F., Klein Goldewijk, K., Körtzinger, A., Landschützer, P.,
465 Lefèvre, N., Lenton, A., Lienert, S., Lima, I., Lombardozzi, D., Metzl, N., Millero, F., Monteiro, P. M. S., Munro, D. R., Nabel, J. E. M. S., Nakaoka, S.-I., Nojiri, Y., Padin, X. A., Peregon, A., Pfeil, B., Pierrot, D., Poulter, B., Rehder, G., Reimer, J., Rödenbeck, C., Schwinger, J., Séférian, R., Skjelvan, I., Stocker, B. D., Tian, H., Tilbrook, B., Tubiello, F. N., van der Laan-Luijkx, I. T., van der Werf, G. R., van Heuven, S., Viovy, N., Vuichard, N., Walker, A. P., Watson, A. J., Wiltshire, A. J., Zaehle, S., and Zhu, D.: Global Carbon Budget 2017, Earth System Science Data, 10, 405–448, https://doi.org/10.5194/essd-10-405-2018, 2018.

470 Lenton, A. and Matear, R.: Role of the Southern Annular Mode (SAM) in Southern Ocean CO_2 uptake, Global Biogeochemical Cycles, 21, doi:10.1029/2006GB002 714, 2007.

LeQuéré, C., Rödenbeck, C., Buitenhuis, E., Conway, T., Langenfelds, R., Gomez, A., Labuschagne, C., Ramonet, M., Nakazawa, T., Metzl, N., Gillett, N., and Heimann, M.: Saturation of the Southern Ocean CO_2 sink due to recent climate change, Science, 316, 1735–1738, 2007.

475 Li, H. and Ilyina, T.: Current and Future Decadal Trends in the Oceanic Carbon Uptake Are Dominated by Internal Variability, Geophysical Research Letters, 45, 916–925, https://doi.org/10.1002/2017GL075370, 2018.

Locarnini, R., Mishonov, A., Antonov, J., Boyer, T., Garcia, H., Baranova, O. K., Zweng, M. M., Paver, C. R., Reagan, J. R., Johnson, D. R., Hamilton, M., and Seidov, D.: World Ocean Atlas 2013, vol. 1, chap. Temperature, p. 40, Ed. NOAA Atlas NESDIS 73, U.S. Government Printing Office, Washington, D.C., 2013.

480 Lovenduski, N., Gruber, N., Doney, S., and Lima, I.: Enhanced CO_2 outgassing in the Southern Ocean from a positive phase of the Southern Annular Mode, Global Biogeochemical Cycles, 21, doi:10.1029/2006GB002 900, 2007.

Lovenduski, N., Gruber, N., and Doney, S.: Toward a mechanistic understanding of the decadal trends in the Southern Ocean carbon sink, Global Biogeochemical Cycles, 22, doi:10.1029/2007GB003 139, 2008.

Lu, J. and Speer, K.: Topography, jets, and eddy mixing in the Southern Ocean, Journal of Marine Research, 68, 479–502, https://doi.org/10.1357/002224010794657227, 2010.

Mackallah, C., Chamberlain, M., Law, R., Dix, M., Ziehn, T., Bi, D., Bodman, R., Brown, J., Dobrohotoff, P., Druken, K., Evans, B., Harman, I., Hayashida, H., Holmes, R., Kiss, A., Lenton, A., Liu, Y., Marsland, S., Meissner, K., Menviel, L., O'Farrell, S., Rashid, H., Ridzwan, S., Savita, A., Srbinovsky, J., Sullivan, A., Trenham, C., Vohralik, P., Wang, Y.-P., Williams, G., Woodhouse, M., and Yeung, N.: ACCESS datasets for CMIP6: methodology and idealised experiments, Journal of Southern Hemisphere Earth Systems Science, 72, 93–116, https://doi.org/10.1071/ES21031, 2022.

Marshall, G.: Trends in the Southern Annular Mode from observations and reanalyses, J. Clim., 16, 4134–4143, 2003.

Matear, R. and Lenton, A.: Impact of Historical Climate Change on the Southern Ocean Carbon Cycle, Journal of Climate, 21, 5820–5834, https://doi.org/10.1175/2008JCLI2194.1, 2008.

McKinley, G. A., Fay, A. R., Eddebbar, Y. A., Gloege, L., and Lovenduski, N. S.: External Forcing Explains Recent Decadal Variability of the Ocean Carbon Sink, AGU Advances, 1, e2019AV000 149, https://doi.org/10.1029/2019AV000149, e2019AV000149 2019AV000149, 2020.

Menviel, L., Timmermann, A., Mouchet, A., and Timm, O.: Climate and marine carbon cycle response to changes in the strength of the southern hemispheric westerlies, Paleoceanography, 23, doi:10.1029/2007PA001 604, 2008.

Menviel, L., Spence, P., Yu, J., Chamberlain, M., Matear, R., Meissner, K., and England, M.: Southern Hemisphere westerlies as a driver of the early deglacial atmospheric CO_2 rise, Nature Communications, 9, 2503, https://doi.org/10.1038/s41467-018-04876-4, 2018.

Mikaloff-Fletcher, S., Gruber, N., Jacobson, A., Doney, S., Dutkiewicz, S., Gerber, M., Follows, M., Joos, F., Lindsay, K., Menemenlis, D., Mouchet, A., Müller, S., and Sarmiento, J.: Inverse estimates of anthropogenic CO_2 uptake, tranport, and storage by the ocean, Global Biogeochemical Cycles, 20, GB2002, https://doi.org/10.1029/2005GB002530, 2006.

Morrison, A. and Hogg, A.: On the Relationship between Southern Ocean Overturning and ACC Transport, J. Phys. Oceanogr., 43, 140–148, https://doi.org/10.1175/JPO-D-12-057.1, 2013.

Morrison, A. K., Hogg, A. M., England, M. H., and Spence, P.: Warm Circumpolar Deep Water transport toward Antarctica driven by local dense water export in canyons, Science Advances, 6, eaav2516, https://doi.org/10.1126/sciadv.aav2516, 2020.

Munday, D. R., Johnson, H. L., and Marshall, D. P.: Eddy Saturation of Equilibrated Circumpolar Currents, Journal of Physical Oceanography, 43, 507 – 532, https://doi.org/10.1175/JPO-D-12-095.1, 2013.

Munday, D. R., Johnson, H. L., and Marshall, D. P.: Impacts and effects of mesoscale ocean eddies on ocean carbon storage and atmospheric pCO2, Global Biogeochemical Cycles, 28, 877–896, https://doi.org/10.1002/2014GB004836, 2014.

Oke, P., Griffin, D., Schiller, A., Matear, R., Fiedler, R., Mansbridge, J., Lenton, A., Cahill, M., Chamberlain, M., and Ridgway, K.: Evaluation of a near-global eddy-resolving ocean model, Geoscience Model Development, 6, 591–615, https://doi.org/10.5194/gmd-6-591-2013, 2013.

Olsen, A., Key, R. M., van Heuven, S., Lauvset, S. K., Velo, A., Lin, X., Schirnick, C., Kozyr, A., Tanhua, T., Hoppema, M., Jutterstrom, S., Steinfeldt, R., Jeansson, E., Ishii, M., Pérez, F. F., and Suzuki., T.: The Global Ocean Data Analysis Project version 2 (GLODAPv2) - an internally consistent data product for the world ocean, Earth System Science Data, 8, 297–323, 2016.

Orr, J. C., Najjar, R. G., Aumont, O., Bopp, L., Bullister, J. L., Danabasoglu, G., Doney, S. C., Dunne, J. P., Dutay, J.-C., Graven, H., Griffies, S. M., John, J. G., Joos, F., Levin, I., Lindsay, K., Matear, R. J., McKinley, G. A., Mouchet, A., Oschlies, A., Romanou, A., Schlitzer, R.,

520   Tagliabue, A., Tanhua, T., and Yool, A.: Biogeochemical protocols and diagnostics for the CMIP6 Ocean Model Intercomparison Project (OMIP), Geoscientific Model Development, 10, 2169–2199, https://doi.org/10.5194/gmd-10-2169-2017, 2017.

Prend, C. J., Gray, A. R., Talley, L. D., Gille, S. T., Haumann, F. A., Johnson, K. S., Riser, S. C., Rosso, I., Sauvé, J., and Sarmiento, J. L.: Indo-Pacific Sector Dominates Southern Ocean Carbon Outgassing, Global Biogeochemical Cycles, 36, e2021GB007 226, https://doi.org/10.1029/2021GB007226, 2022.

525   Ritter, R., Landschützer, P., Gruber, N., Fay, A. R., Iida, Y., Jones, S., Nakaoka, S., Park, G.-H., Peylin, P., Rödenbeck, C., Rodgers, K. B., Shutler, J. D., and Zeng, J.: Observation-Based Trends of the Southern Ocean Carbon Sink, Geophysical Research Letters, 44, 12,339–12,348, https://doi.org/10.1002/2017GL074837, 2017.

Sabine, C., Feely, R., Gruber, N., Key, R., Lee, K., Bullister, J., Wanninkhof, R., Wong, C., Wallace, D., Tilbrook, B., Millero, F., Peng, T.-H., Kozyr, A., Ono, T., and Rios, A.: The oceanic sink of anthropogenic CO_2, Science, 305, 367–371, 2004.

530   Sarmiento, J. and Gruber, N.: Ocean Biogeochemical Dynamics, vol. 526pp, Princeton University Press, Princeton, NJ, 2006.

Sokolov, S. and Rintoul, S. R.: Circumpolar structure and distribution of the Antarctic Circumpolar Current fronts: 1. Mean circumpolar paths, Journal of Geophysical Research: Oceans, 114, https://doi.org/10.1029/2008JC005108, 2009.

Solodoch, A., Stewart, A. L., Hogg, A. M., Morrison, A. K., Kiss, A. E., Thompson, A. F., Purkey, S. G., and Cimoli, L.: How Does Antarctic Bottom Water Cross the Southern Ocean?, Geophysical Research Letters, 49, e2021GL097 211, https://doi.org/10.1029/2021GL097211,

535   2022.

Spence, P., Fyfe, J. C., Montenegro, A., and Weaver, A. J.: Southern Ocean response to strenghening winds in an eddy-permitting global climate model, J. Climate, 23, 5332–5343, https://doi.org/https://doi.org/10.1175/2010JCLI3098.1, 2010.

Stewart, K. D., Hogg, A., England, M. H., and Waugh, D. W.: Response of the Southern Ocean Overturning Circulation to Extreme Southern Annular Mode Conditions, Geophysical Research Letters, 47, e2020GL091 103, https://doi.org/10.1029/2020GL091103, 2020.

540   Tagliabue, A., Aumont, O., DeAth, R., Dunne, J. P., Dutkiewicz, S., Galbraith, E., Misumi, K., Moore, J. K., Ridgwell, A., Sherman, E., Stock, C., Vichi, M., Völker, C., and Yool, A.: How well do global ocean biogeochemistry models simulate dissolved iron distributions?, Global Biogeochemical Cycles, 30, 149–174, https://doi.org/10.1002/2015GB005289, 2016.

Thompson, D. and Solomon, S.: Interpretation of recent southern hemisphere climate change, Science, 296, 895–899, 2002.

Toggweiler, J.: Variation of atmospheric CO_2 by ventilation of the ocean's deepest water, Paleoceanography, 14, 571–588, 1999.

545   Tsujino, H., Urakawa, S., Nakano, H., Small, R. J., Kim, W. M., Yeager, S. G., Danabasoglu, G., Suzuki, T., Bamber, J. L., Bentsen, M., Böning, C. W., Bozec, A., Chassignet, E. P., Curchitser, E., Boeira Dias, F., Durack, P. J., Griffies, S. M., Harada, Y., Ilicak, M., Josey, S. A., Kobayashi, C., Kobayashi, S., Komuro, Y., Large, W. G., Le Sommer, J., Marsland, S. J., Masina, S., Scheinert, M., Tomita, H., Valdivieso, M., and Yamazaki, D.: JRA-55 based surface dataset for driving ocean–sea-ice models (JRA55-do), Ocean Modelling, 130, 79–139, https://doi.org/10.1016/j.ocemod.2018.07.002, 2018.

550   Völker, C. and Köhler, P.: Responses of ocean circulation and carbon cycle to changes in the position of the Southern Hemisphere westerlies at Last Glacial Maximum, Paleoceanography, 28, 726–739, https://doi.org/10.1002/2013PA002556, 2013.

Wanninkhof, R.: Relationship between gas exchange and wind speed over the ocean, Journal of Geophysical Research, 97, 7373–7381, 1992.

Waugh, D. W. and Haine, T. W. N.: How Rapidly Do the Southern Subtropical Oceans Respond to Wind Stress Changes?, Journal of Geophysical Research: Oceans, 125, e2020JC016 236, https://doi.org/10.1029/2020JC016236, e2020JC016236 2020JC016236, 2020.

555   Waugh, D. W., Banerjee, A., Fyfe, J. C., and Polvani, L. M.: Contrasting Recent Trends in Southern Hemisphere Westerlies Across Different Ocean Basins, Geophysical Research Letters, 47, e2020GL088 890, https://doi.org/10.1029/2020GL088890, 2020.

Ziehn, T., Chamberlain, M. A., Law, R. M., Lenton, A., Bodman, R. W., Dix, M., Stevens, L., Wang, Y.-P., and Srbinovsky, J.: The Australian
Earth System Model: ACCESS-ESM1.5, Journal of Southern Hemisphere Earth Systems Science, https://doi.org/10.1071/ES19035, 2020.
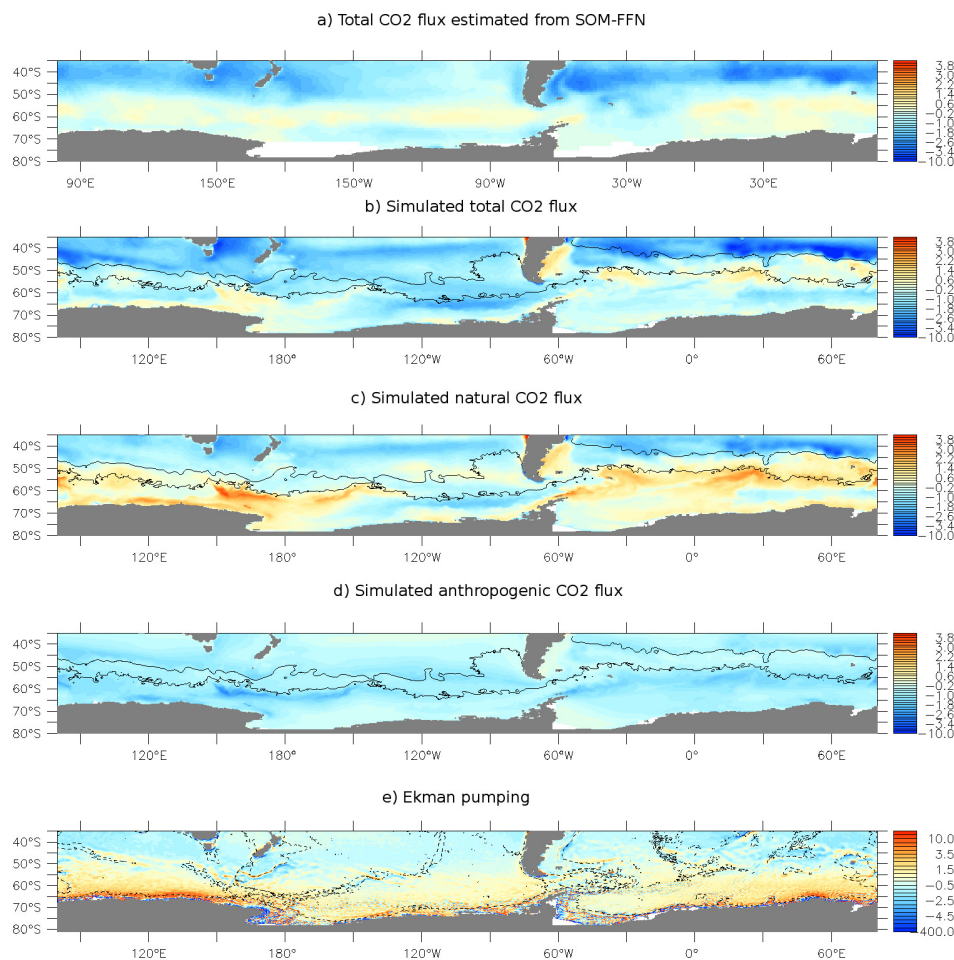
Figure 1. a) Total ocean to atmosphere CO_2 flux (molC/m^2/yr) as estimated from the SOM-FFN for the period 1982-2021 (Landschützer et al., 2015). Simulated b) Total, c) natural and d) anthropogenic ocean to atmosphere CO_2 flux (molC/m^2/yr) averaged over the period 1982-2021. The black contours indicate (from south to north) the northern edges of the PF and SAF using the definition of Sokolov and Rintoul (2009). e) Ekman pumping (x10^{-6} m/s) averaged over the period 1982-2021 in the numerical experiment. The black lines overlaid represent the 2500m depth bathymetry contour.
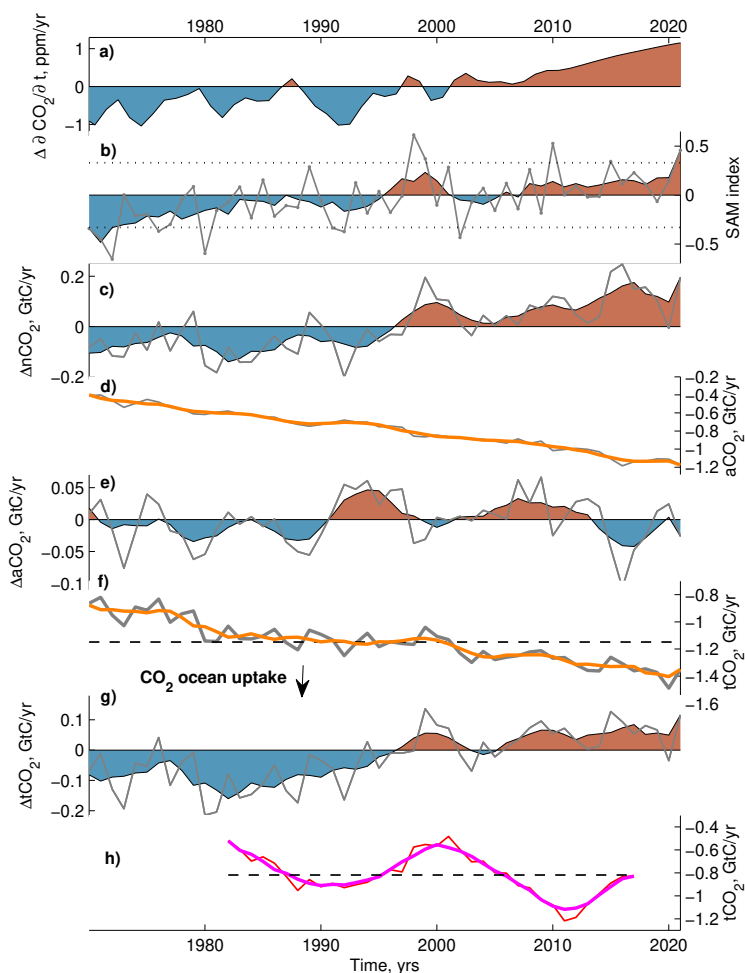
Figure 2. Time series of a) annual mean atmospheric CO_2 growth rate (ppm/yr) used as forcing, b) SAM index calculated from the JRA55-do dataset (Stewart et al., 2020), simulated ocean to atmosphere integrated c) nCO_2 anomalies with respect to the 1970-2021 mean, d) aCO_2, e) detrended aCO_2 anomalies with respect to the 1970-2021 mean, f) tCO_2 and g) detrended tCO_2 anomalies with respect to the 1970-2021 mean. h) SO tCO_2 flux (GtC/yr) as derived from the SOM-FFN (Landschützer et al., 2019; Bushinsky et al., 2019). All the CO_2 fluxes are integrated over the SO (35°S-80°S) and are in GtC/yr. Light lines represent annual mean values, thick lines represent the 5-yr running means, and dashed horizontal lines represent the mean over the available period. For the SAM index, the horizontal dashed and dotted lines represent the thresholds used to define positive and neutral SAM in the composites.
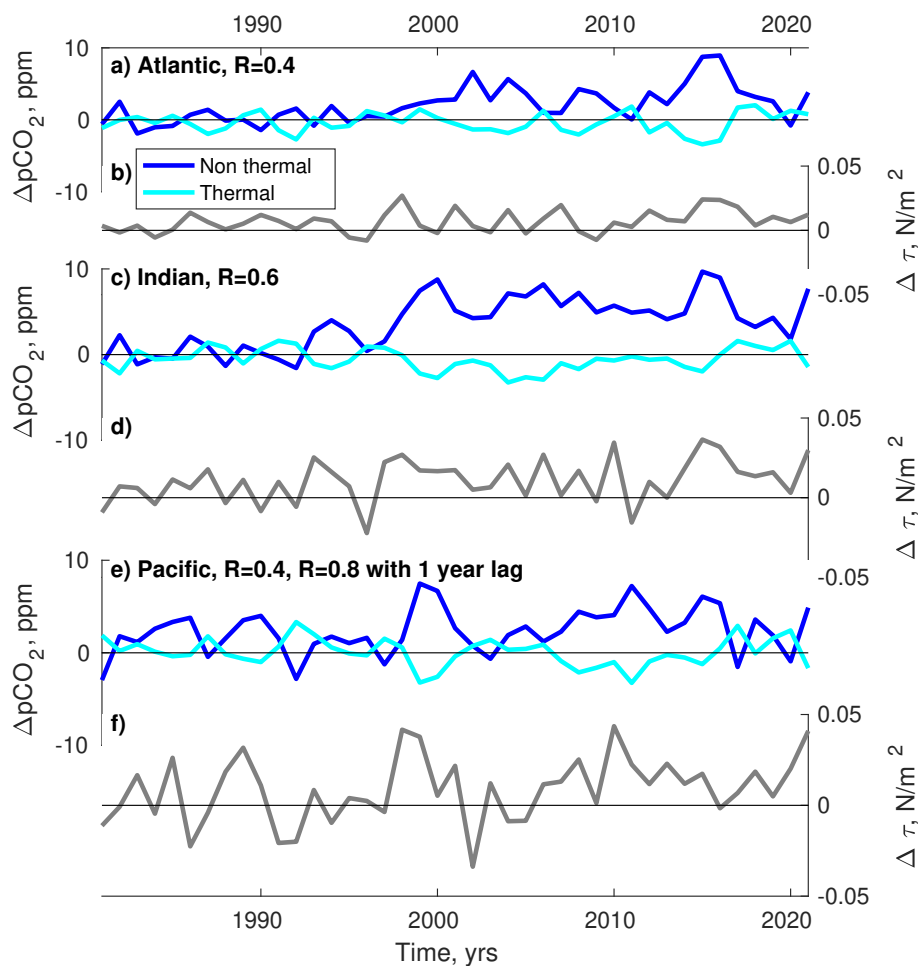
Figure 3. a) Non thermal (blue) and thermal (cyan) pCO$_2$ contributions anomalies (ppm) south of 50°S and b) maximum zonal wind stress anomalies (N/m^2) with respect to the 1980-1982 mean over the Atlantic sector (70°W-20°E). c-d) Same as a-b) for the Indian sector (20°E-130°E). e-f) Same as a-b) for the Pacific sector (130°E-70°W). The correlation coefficients between the non-thermal pCO$_2$ variations and the wind stress changes are indicated for each sector.
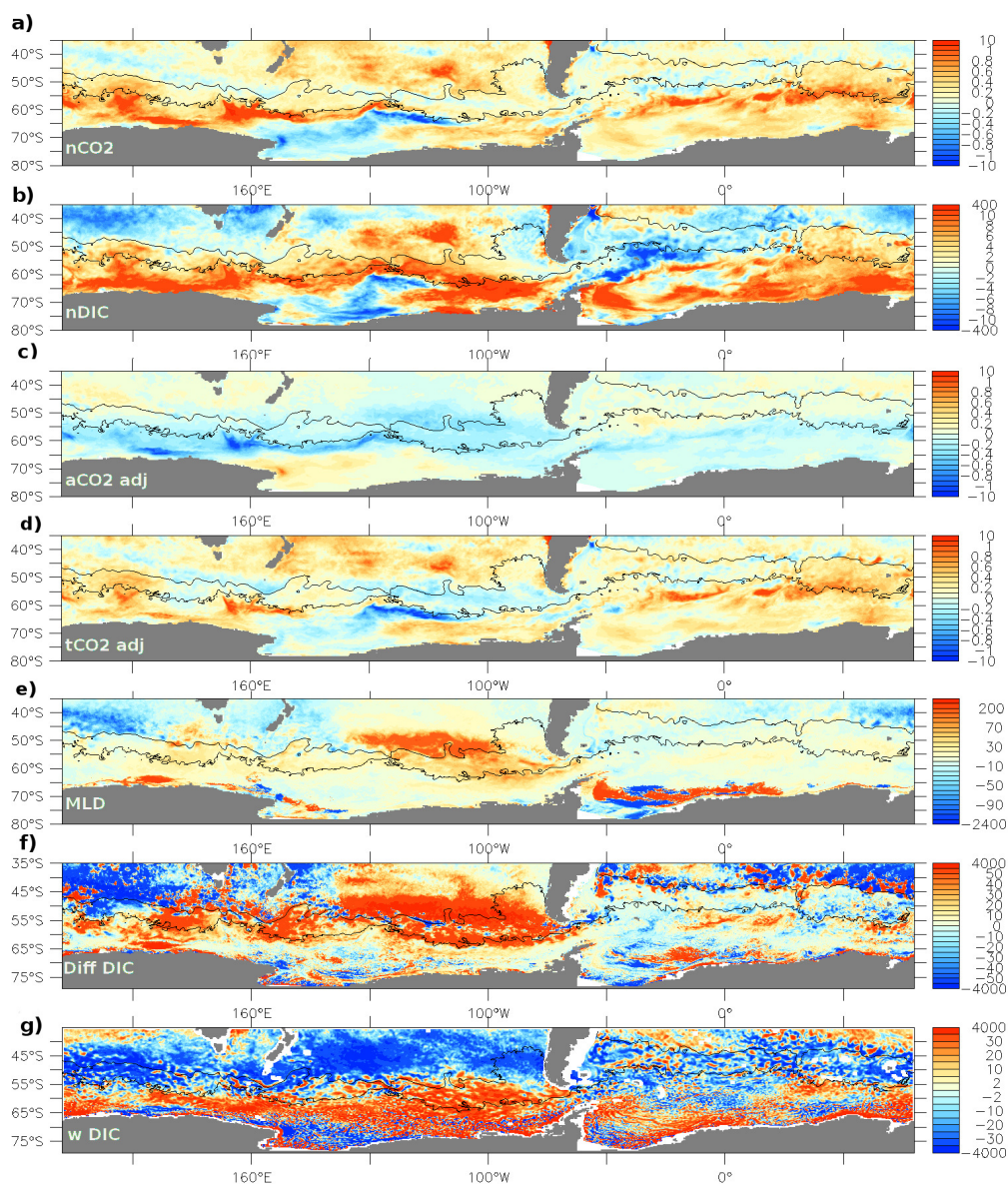
Figure 4. a) nCO_2 flux (mol/m^2/yr), b) surface nDIC (mmol/m^3), c) adjusted aCO_2 flux (mol/m^2/yr) and d) adjusted tCO_2 flux (mol/m^2/yr) anomalies for a composite of positive phases of the SAM ($\geq$0.83, i.e. 1998, 1999, 2010, 2015 and 2021) compared to a composite of negative SAM years (1980, 1991, 1992, 2002). Linear trends in aCO_2 fluxes have been removed from the aCO_2 and tCO_2 anomalies to take into account the difference in mean years between the composite of positive and negative SAM years. Annual average anomalies of e) maximum monthly mixed layer depth (m), f) vertical diffusivity multiplied by the DIC gradient at the base of mixed layer (mol/m^2/yr) and g) vertical Ekman DIC advection with a 21 point smoothing (mol/m^2/yr), for positive phases of the SAM compared to negative SAM years.
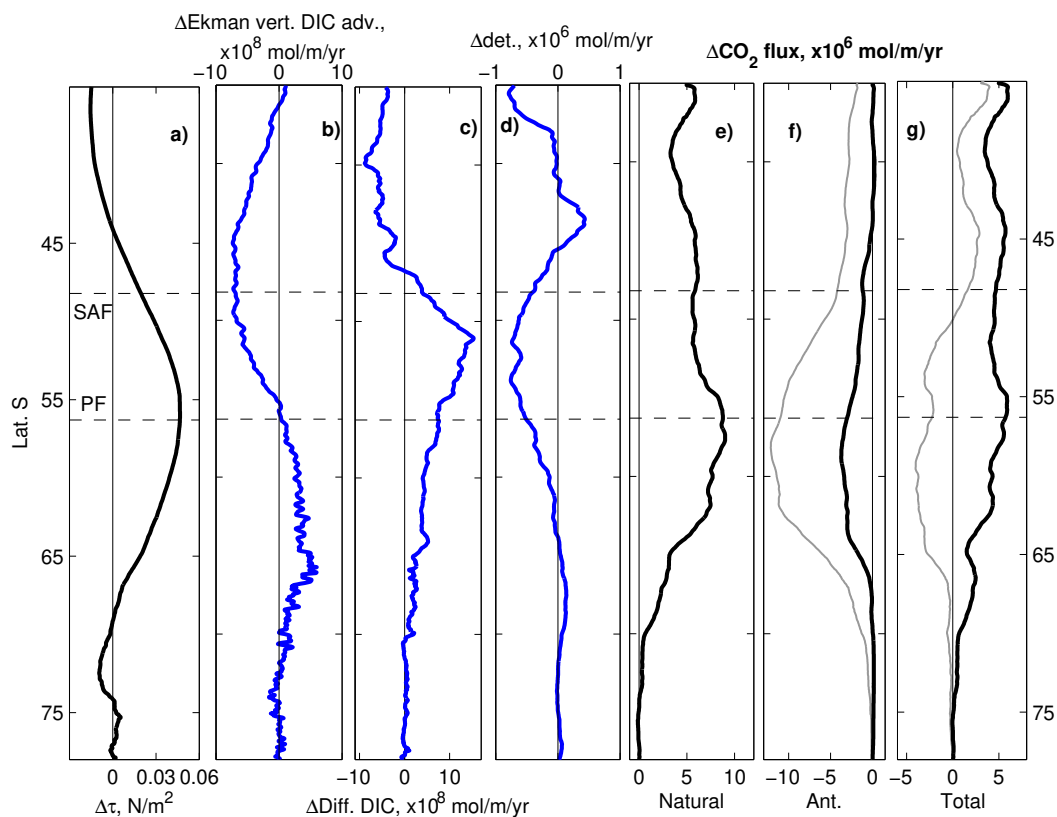
Figure 5. a) Zonally averaged wind stress anomalies (N/m^2); Anomalies in zonally integrated b) vertical Ekman DIC advection (x10^8 mol/m/yr), c) vertical diffusivity multiplied by the DIC gradient at the base of mixed layer (x10^8 mol/m/yr), d) detritus flux at 100m depth (x10^6 mol/m/yr), e) nCO$_2$, f) aCO$_2$ and g) tCO$_2$ total for the positive SAM composite compared to the negative SAM composite. In f and g) the grey lines represent the actual data and the black lines include a correction for the fact that the SAM composite represents more recent years than the negative SAM composite.
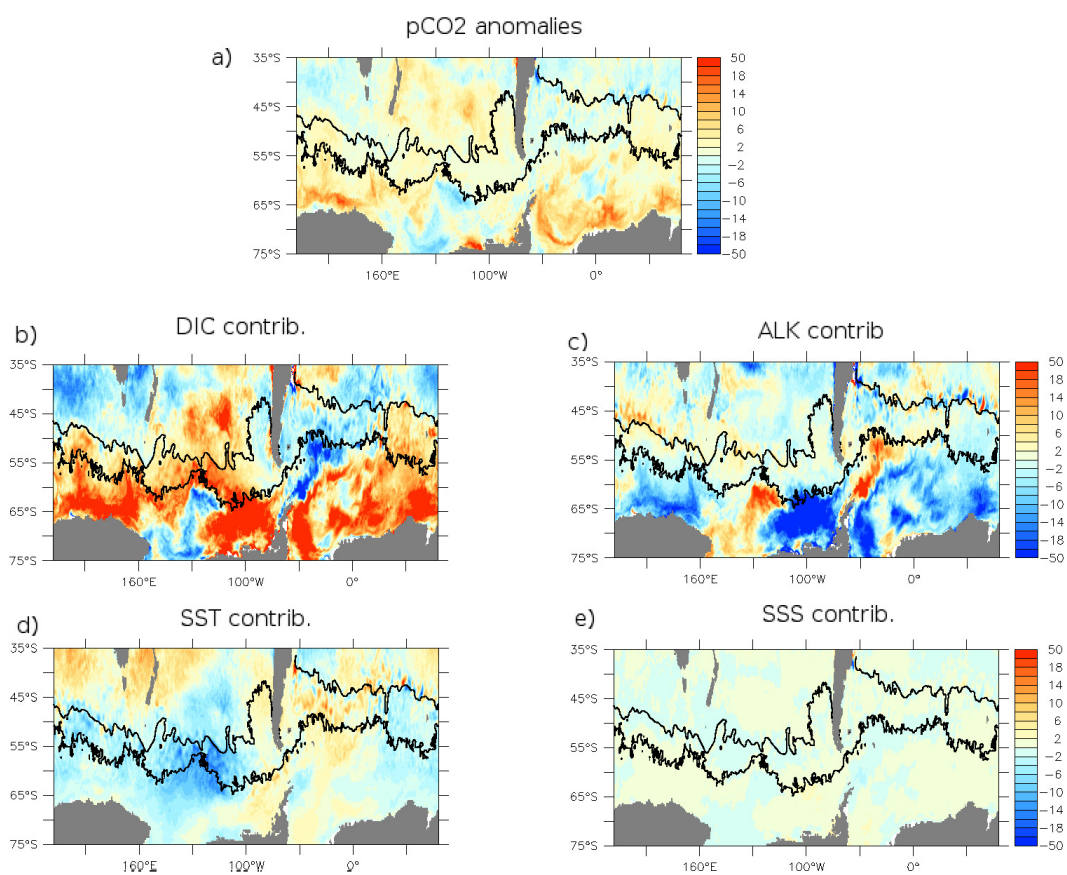
Figure 6. Surface ocean a) pCO$_2$ anomalies (ppm) for positive phases of the SAM compared to a composite of negative SAM years and the pCO$_2$ contributions (ppm) from b) DIC, c) ALK, d) SST and e) SSS.
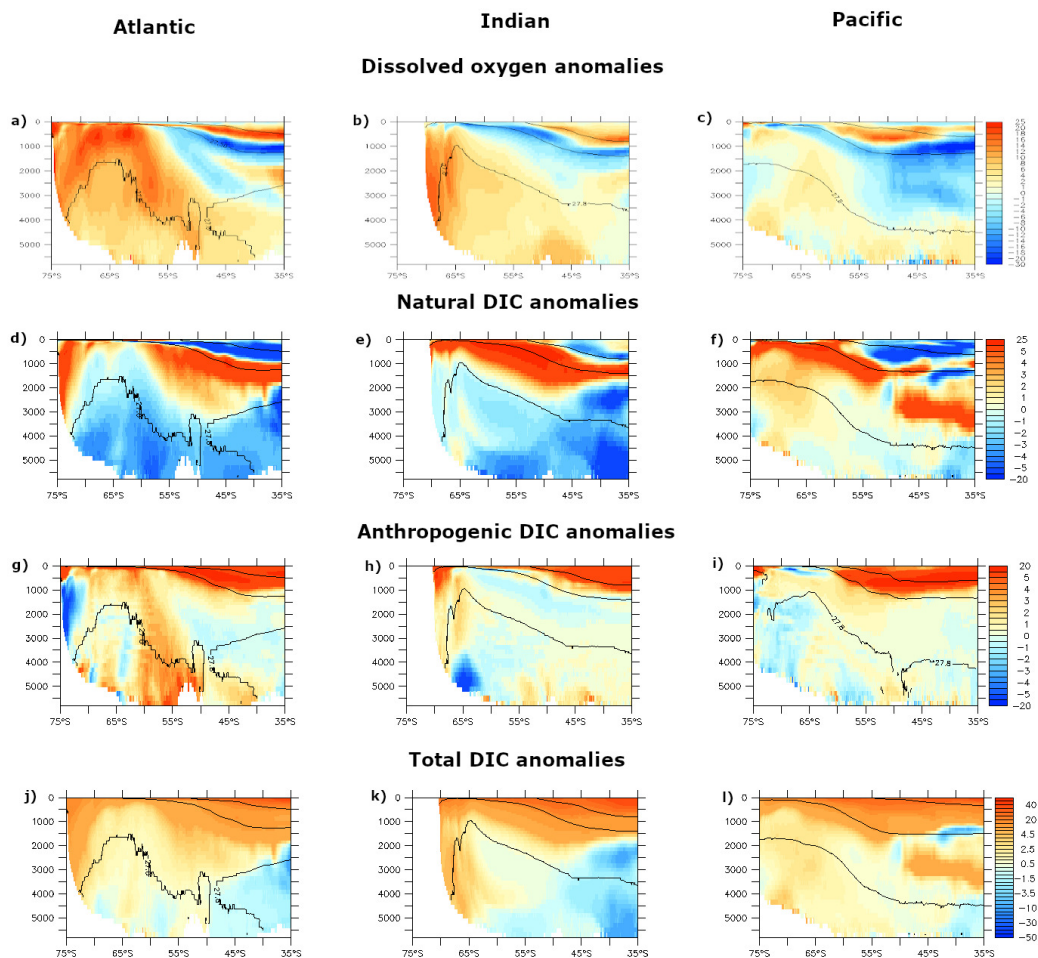
Figure 7. Zonally averaged (a-c) dissolved O_2 (mmol/m^3), (d-f) natural DIC, (g-i) anthropogenic DIC and (j-l) total DIC anomalies (mmol/m^3) averaged over (left) the Atlantic, (middle) the Indian and (right) the Pacific for years 2017-2021 compared to 1980-1982. The density of the AABW ($\geq$1028.31 kg/m^3), the AAIW (1027.5$\geq$AAIW$\geq$1026.95 kg/m^3) and the SAMW ($\leq$1026.95 kg/m^3) are overlaid. For anthropogenic DIC, the anomalies represent the deviation from the linear accumulation of anthropogenic DIC following the pattern obtained during the 1970s Gruber et al. (2019a). The total DIC anomalies represent the sum of the natural and anthropogenic DIC anomalies.
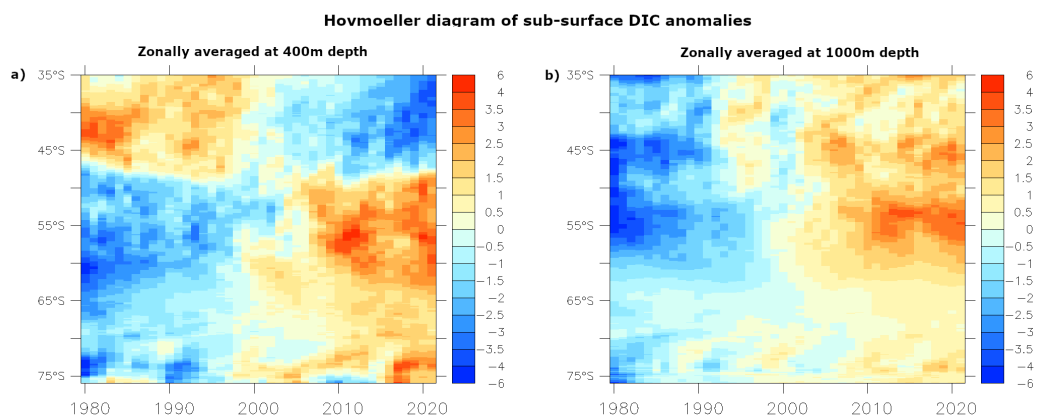
Figure 8. Hovmoeller diagram of zonally averaged nDIC anomalies (mmol/m^3) as a function of time and latitude at a) 400 m and b) 1000 m depth compared to the time average nDIC.